scientific reports

Check for updates

OPEN

Optimization of the plasmonic properties of titanium nitride films sputtered at room temperature through microstructure and thickness control

Mateusz Nieborek[1], Cezariusz Jastrzębski[2], Tomasz Płociński[3], Piotr Wróbel[4], Aleksandra Seweryn[5] & Jarosław Judek[1]✉

A current approach to depositing highly plasmonic titanium nitride films using the magnetron sputtering technique assumes that the process is performed at temperatures high enough to ensure the atoms have sufficient diffusivities to form dense and highly crystalline films. In this work, we demonstrate that the plasmonic properties of TiN films can be efficiently tuned even without intentional substrate heating by influencing the details of the deposition process and entailed films' stoichiometry and microstructure. We also discuss the dependence of the deposition time/films' thickness on the optical properties, which is another degree of freedom in controlling the optical response of the refractory metal nitride films. The proposed strategy allows for robust and cost-effective production of large-scale substrates with good plasmonic properties in a CMOS technology-compatible process that can be further processed, e.g., structurized. All reported films are characterized by the maximal values of the plasmonic Figure of Merit (FoM = $-\varepsilon_1/\varepsilon_2$) ranging from 0.8 to 2.6, and the sample with the best plasmonic properties is characterized by FoM at 700 nm and 1550 nm that is equal 2.1 in both cases. These are outstanding results, considering the films' polycrystallinity and deposition at room temperature onto a non-matched substrate.

Titanium nitride belongs to an interesting class of plasmonic materials working in the ultraviolet, visible, and infrared spectral ranges and called refractory metal nitrides[1–3]. Despite generally worse plasmonic properties (a less negative real part ε_1 and a more positive imaginary part ε_2 of the dielectric function) than typically used noble metals like gold or silver, TiN poses some unique attributes that still make it attractive for photonic applications[4]. The most important feature is the compatibility with silicon technology, understood both as compatibility of the materials and fabrication techniques. Consequently, photonic structures or devices containing TiN as the plasmonic component could be potentially fabricated within existing industrial production lines, making the implementation straightforward and economically advantageous. The resistance to elevated temperatures, far higher than gold's and silver's melting temperatures, is another interesting and unique feature of this refractory metal nitride[5]. Decomposition temperatures reaching 2900 °C and the possibility of preservation of the optical properties up to even 1000 °C[6–9] pave the way for applications requiring high operating temperatures[10–12]. Additionally, when considering the high abundance of constituent elements—titanium and nitrogen, in Earth's crust, cheap manufacturing methods, non-toxicity, and biological compatibility—titanium nitride appears to be a very economically and environmentally attractive plasmonic material.

Successful depositions of titanium nitride films with plasmonic properties have been widely reported in recent years. Among deposition techniques, one can include atomic layer deposition[13–16], pulsed laser deposition[17,18], molecular beam epitaxy[19,20] and magnetron sputtering[21–27]. The deposition was performed onto a broad class

[1]Institute of Microelectronics and Optoelectronics, Warsaw University of Technology, Koszykowa 75, 00-662 Warsaw, Poland. [2]Faculty of Physics, Warsaw University of Technology, Koszykowa 75, 00-662 Warsaw, Poland. [3]Faculty of Materials Science and Engineering, Warsaw University of Technology, Wołoska 141, 02-507 Warsaw, Poland. [4]Faculty of Physics, University of Warsaw, Pasteura 5, 02-093 Warsaw, Poland. [5]Institute of Physics, Polish Academy of Sciences, Aleja Lotników 32/46, 02-668 Warsaw, Poland. ✉email: jaroslaw.judek@pw.edu.pl

of substrates, including rigid and flexible substrates[28], substrates that are crystallographically matched (e.g., MgO[29]), unmatched (e.g., silicon[30]), or intentionally highly mismatched[31], and even on polymers like PMMA[24]. The range of the substrate temperatures during depositions starts from room temperature to as high values as 1000[28]–1100 °C[31]. Typically, high-temperature epitaxy on a crystallographically matched substrate is expected to provide films with the best plasmonic properties. This fact might be, however, somehow problematic since high-temperature processes are not always possible or economically justified. For example, high-temperature processing is incompatible with complementary metal–oxide–semiconductor fabrication. In such cases, low-temperature deposition, particularly deposition at room temperature, might be the only reasonable choice. As regards the magnetron sputtering of plasmonic titanium nitride at room temperature, the following variations of the deposition were reported: (1) DC magnetron sputtering on Si(100)[21], (2) DC magnetron sputtering on MgO(100), c-plane sapphire, and Si(100)[22], (3) the high-power impulse magnetron sputtering onto B270 glass[23], (4) RF bias-free sputtering onto Si, quartz, HfO_2, and PMMA[24], (5) pulsed-DC sputtering with additional RF substrate biasing on soda-lime glass and Si(111)[25], and (6) reactive high-power impulse magnetron sputtering (R-HiPIMS) with glancing angle deposition (GLAD) on silicon (Si) wafer (100)[26].

In this work, we show a strategy for optimizing the plasmonic properties of relatively thick/nontransparent polycrystalline titanium nitride films deposited using the pulsed-DC reactive magnetron sputtering technique at room temperature on a non-matched substrate, i.e., Si(100) wafer with a 10 nm thick TiO_x interlayer. Application of the dielectric buffer layer decreases the films' stress, allowing for successful TiN deposition on 4" Si wafers. The main advancement we report is the demonstration that the plasmonic properties of titanium nitride films can be efficiently tuned even without intentional heating by influencing the details of the deposition process and entailed films' stoichiometry and microstructure by controlling the working pressure and gas flows. We also discuss the dependence of the deposition time/films' thickness on the optical properties, which is another degree of freedom in controlling the optical response of the titanium nitride films[16,32,33].

Our idea/strategy can be understood within the framework of modern structure zone models (SZM), which try to relate films' microstructures and the parameters of the physical vapor deposition processes. Historically, the idea of SZM was first introduced by Movchan and Demchishin, who noticed that the critical parameter determining the films' microstructures is the ratio of the substrate temperature during the deposition process to the material's melting temperature. The so-called homologous temperature translates into the adatoms' surface mobility/diffusivity, directly determining what microstructure will be formed. In their work, Movchan and Demchishin identified/distinguished three types of possible microstructure that can be formed depending on the homologous temperature value[34]. Next, Thornton extended the SZM by noticing the importance of working gas pressure[35], whereas Mahieu raised a question concerning the energy and atomic fluxes towards the substrate[36,37]. Finally, Anders generalized the SZM by suggesting that the homologous temperature should be replaced by "a generalized temperature, which includes the homologous temperature plus a temperature shift caused by the potential energy of particles arriving on the surface" and the pressure by "a normalized energy, describing displacement and heating effects caused by the kinetic energy of bombarding particles"[38]. The last sentence seems especially important since the kinetic energy distribution within the particle flux toward the substrate might be the missing link to explain why and how pressure and argon flow influence the film microstructure. We would like to make a digression here. The relation between the pressure and the distribution of the kinetic energy of the particle flux toward a substrate was recently examined in a completely different context. Johansson[39] and Pliatsikas[40] investigated sputter-induced damage to the substrate's surface during the deposition using graphene as the damage indicator. Both publications conclude that the kinetic energy distribution within the Ar ions depends directly on the pressure. At low working pressures, the ballistic damage due to Ar bombardment is the highest due to the increased probability of highly energetic Ar ions within the plasma.

For the sake of order, we note that the complementary study on the influence of substrate temperature on the microstructure and optical properties of titanium nitride films was already reported[41].

Results and discussion

Microstructure and plasmonic properties of titanium nitride films as a function of N_2 and Ar flow values

In the first part of our experiment, we analyze how parameters of the employed physical vapor deposition process, i.e., argon flow, which determines the working pressure, simultaneously with nitrogen flow, influence the stoichiometry, microstructure, and optical properties of the deposited films and if any correlation between these three properties can be noticed. We note that all samples whose properties are reported in this subchapter were deposited with constant time, and in consequence, their thickness varies.

Figure 1 presents data that can be helpful for qualitative analysis. Figure 1a–d shows pictures of four series of samples deposited for four different Ar flow values: 10 sccm, 25 sccm, 50 sccm, and 100 sccm. Within each series, samples are deposited with such nitrogen flow values to get stoichiometric and non-stoichiometric samples, both with nitrogen deficiency and excess. It can be perceived that samples deposited for the lowest nitrogen flow are silver in color, samples deposited for the moderate nitrogen flow have golden luster, whereas samples deposited for the highest nitrogen flow are brownish. It is because changing nitrogen flow for the selected value of the argon flow allows for the stoichiometry control, and stoichiometry-dependent changes in films' color is a typical and widely observed behavior for refractory metal nitrides due to the composition-dependent shift in screened plasma frequency value[42]. Figure 1e–h show SEM images of samples' cross-sections. A vertical columnar structure can be distinguished for all samples, but drawing more precise conclusions about the microstructure is difficult. The exception is the surface topography characterized by faceting, which depends on Ar flow and is most pronounced for the 100 sccm Ar flow value. The increase in surface faceting as the Ar flow increases is rendered in AFM images shown in Fig. 1i–l, also as the increase in surface roughness. To study the microstructure, we

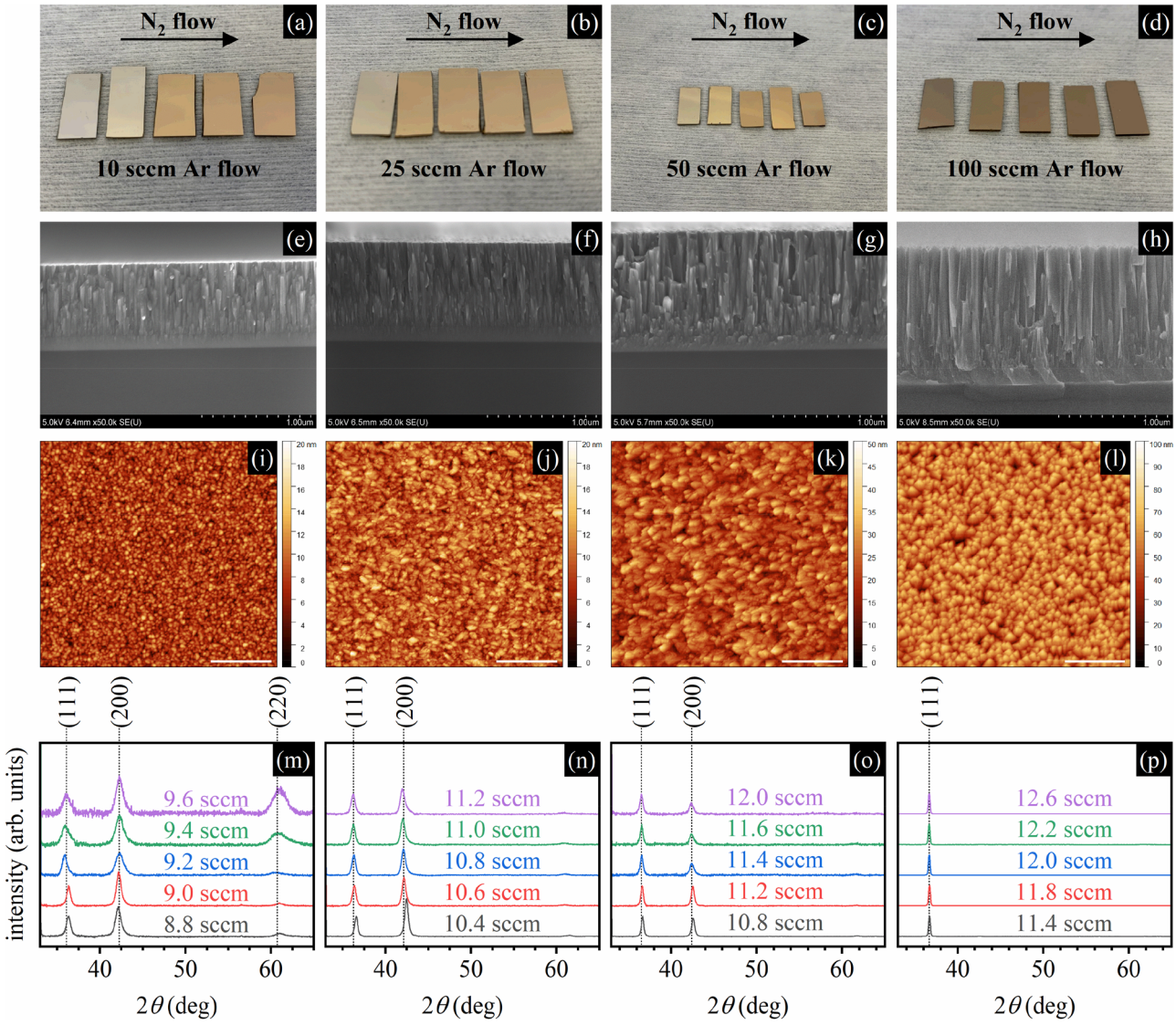

Figure 1. (**a**–**d**) Pictures of four series of TiN samples, five samples each, deposited with different N_2 flows (within the series) and with different Ar flows (between the series); (**e**–**h**) SEM pictures of the most stoichiometric samples from the series; (**i**–**l**) AFM pictures of the surface of the most stoichiometric samples from the series (the length of the scale bar equals 500 nm); (**m**–**p**) XRD patterns for different N_2 (within the plots) and Ar flows (between the plots).

performed the XRD measurements, the results of which are shown in Fig. 1m–p as XRD patterns. The changes in relative (111), (200), and (220) peak intensities related to the changes in crystallographic orientations of the nanocrystallites within the polycrystalline film as well as the peak broadening as the Ar flow decreases, can be easily noticed. Particularly, one can distinguish a transition from one narrow (111) peak acquired from samples deposited with 100 sccm Ar flow to three broad (111), (200), and (220) peaks acquired for samples deposited with 10 sccm Ar flow.

To analyze all these data quantitively, we plotted the deposition rate value estimated from the SEM images, RMS values from AFM images, and nanocrystallite size calculated with the Scherrer equation and relative intensities of the XRD peaks in Fig. 2. Figure 2a reveals a strong dependence of the deposition rate on nitrogen flow for all Ar flow values suggesting that the deposition process of the titanium nitride films in all cases occurs on the border between the metallic and dielectric mode of the sputtering process—in the transient mode. The range of changes in the deposition rate when changing nitrogen flow is qualitatively the same regardless of the Ar flow value. What is changing is only the nitrogen flow value that corresponds to the deposition of the stoichiometric films. This high sensitivity of the deposition rate on nitrogen flow for the selected value of the Ar flow can be explained by the increasing coverage of the titanium target by titanium nitride, known as target poisoning. The high variation in the deposition rate is, however, not very strongly rendered in the surface roughness value depicted in Fig. 2b. In the case of surface roughness, the influence of the nitrogen flow is minor compared to the strong influence of the Ar flow. The XRD results shed more light on this behavior. Figure 2c–f illustrate two simultaneous processes that occur when decreasing the Ar flow (the working pressure): the decrease in the

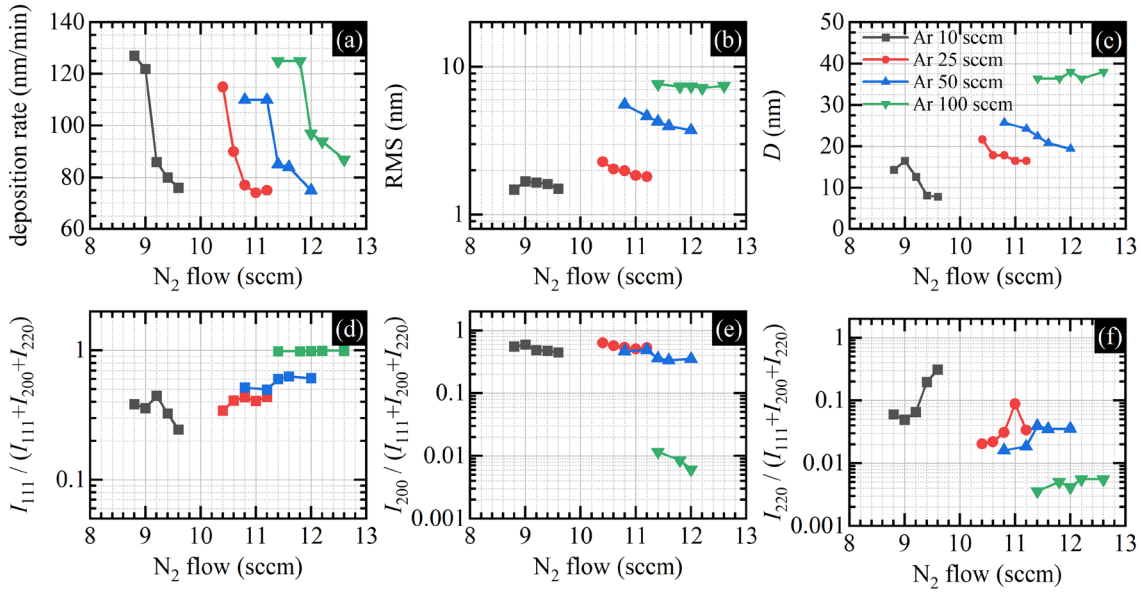

Figure 2. (**a**) Deposition rate; (**b**) RMS; (**c**) nanocrystallite size calculated with Scherrer equation; (**d**) relative intensity of the XRD (111) peak; (**e**) relative intensity of the XRD (200) peak; (**f**) relative intensity of the XRD (220) peak. All data are a function of N_2 flow for different Ar flow values.

nanocrystallite size and the increase in the fraction of other than (111) nanocrystallite orientations. For the highest Ar flow (the highest working pressure of about 0.36 Pa), all nanocrystallites are characterized by an average size of 37 nm and are oriented along (111) orientation despite the samples' stoichiometry. Decreasing the Ar flow to 50 sccm, which results in a decrease in working pressure to 0.15 Pa, leads to a decrease in the average nanocrystallite size to 22 nm and the emergence of a second (200) nanocrystallite orientation. Further decrease of the Ar flow to 25 sccm resulting in working pressure of 0.04 Pa leads to an average nanocrystallite size of 18 nm and further decrease of the (111) nanocrystallites orientation fraction. The lowest Ar flow of 10 sccm results in a working pressure value below 0.013 Pa, nanocrystallite size as small as 8 nm, and the emergence of a distinct (220) peak.

Our interpretation of all these observations is that working pressure control through Ar flow control allows us to change the kinetic energy distribution of the elements constituting the plasma and, consequently, the kinetic energy distribution in the particle flux approaching the substrate, according to modern structure zone models[35–38]. The lower the working pressure, the higher the average kinetic energy of atoms/ions arriving at the film's surface. This kinetic energy can be an additional energy source for the adatoms improving their surface mobility, which should lead to improved crystalline quality of the deposited films. But simultaneously, the high-energy bombardment of the surface may deteriorate its crystalline structure. The extreme case is surface etching[38] due to the bombardment of the surface by high-energy ions/atoms, leading to consequent adatoms removal/ejection. In our case, decreasing the working pressure through the Ar flow value decrease seems not to lead to surface etching, which would manifest as a decrease in the deposition rate. On the contrary, the deposition rate for the lowest Ar flow seems to be higher than for other Ar flow values. Thus, we are not in the etching regime. On the other hand, it seems that the crystalline quality of the films increases neither when decreasing the working pressure since the average nanocrystallite size decreases. We are neither convinced if the emergence of the (200) nanocrystallite orientation, which previously was reported as the positive effect of the higher energy ion bombardment[43] (the (200) surface orientation is characterized by lower surface energy than the (111) one), is a sign of increased crystal quality. We are rather inclined to conclude that we are observing progressive amorphization of the deposited films, understood as the decrease in the average nanocrystallite size and the emergence of random nanocrystallite orientation due to decreased working pressure through the Ar flow value decrease, which results in an increased surface bombardment by high energy ions/atoms. In other words, by changing the working pressure by the Ar flow, we can control the amorphization state of the deposited titanium nitride films by varying the kinetic energy distribution in the particle flux approaching and impacting the substrate. The lower the Ar flow, the lower the pressure and the more highly energetic ions/atoms impact the surface, and thus more amorphous/less crystalline films are deposited.

Optical properties being a result of the ellipsometric measurements are shown in Fig. 3 as the real ε_1 and imaginary ε_2 part of the dielectric function, and the plasmonic Figure of Merit defined as the ratio of the minus real to the imaginary part of the dielectric function $-\varepsilon_1/\varepsilon_2$. All presented traces are dominated by the strong Drude component—a characteristic feature of the metallic titanium nitride with decent plasmonic properties. The free electron contribution manifests as a monotonically decreasing negative value of the ε_1 and a monotonically increasing positive value of ε_2. For plasmonic application, the lower (more negative) value of ε_1, the better; similarly, the lower (less positive) value of ε_2, the better. The plasmonic figure of merit defined above is a value related to the localized surface plasmon resonance phenomena and it is one of the most popular choices for

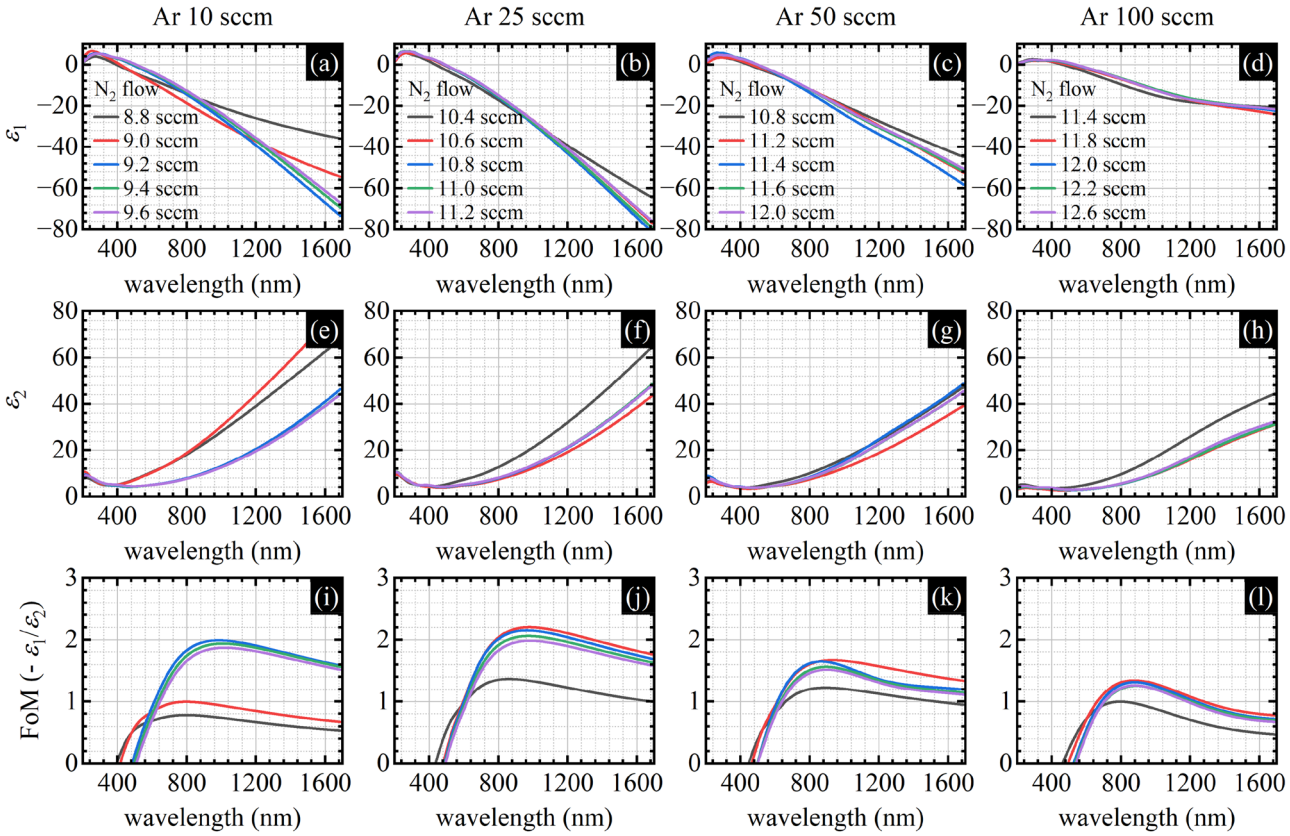

Figure 3. (**a**–**d**) Real ε_1 part of the dielectric function, (**e**–**h**) imaginary ε_2 part of the dielectric function, and (**i**–**l**) plasmonic Figure of Merit ($-\varepsilon_1/\varepsilon_2$) as a function of the wavelength for different N_2 (within the plots) and Ar flows (between the plots).

comparing plasmonic materials. However, choosing other, more application-specific Figures of Merit is also possible[44]. To compare the optical properties more quantitively, we plotted selected parameters calculated from the dielectric function in Fig. 4.

Figure 4a illustrates the wavelength at which the real part of the dielectric function equals zero as a function of nitrogen flow for selected values of Ar flow. Since there is a strong correlation between the $\lambda@\varepsilon_1 = 0$ and the stoichiometry[42], deposited titanium nitride films are stoichiometric (480 nm) and non-stoichiometric, both with the nitrogen excess ($\lambda > 480$ nm), and the deficiency ($\lambda < 480$ nm), for every Ar flow value. Samples deposited with the lowest nitrogen flow value within selected Ar flow have nitrogen deficiency, whereas samples deposited with the highest nitrogen flow value within selected Ar flow have nitrogen excess. Figure 4b illustrates the value of the imaginary part of the dielectric function at the same wavelength at which the real part equals zero. In our case, when the deposition process is performed with constant time, the lowest values are achieved for the most stoichiometric samples. The plasmonic figure of merit is shown in Fig. 4c. As can be seen, the FoM takes the highest values for the most stoichiometric samples within each of the Ar series, but between the series, the FoM for samples deposited with Ar flow that equals 25 sccm takes the highest values. These are very interesting results since, whereas the fact that stoichiometric samples have the best plasmonic properties is somehow intuitive, the existence of the optimum value of the Ar flow that controls the working pressure, for which plasmonic properties are the best, is surprising. Similarly surprising is that the samples deposited with 100 sccm Ar, which are the most crystalline, have the worst plasmonic properties. And the improvement of the plasmonic properties correlates with the progressive amorphization of the films due to the decrease of the working pressure, at least to some critical point (Ar 25 sccm), after which the optical properties deteriorate (Ar 10 sccm). Similar conclusions can be drawn by analyzing the parameters of the Drude component of the dielectric function, which governs the optical properties of TiN in the infrared range: the plasma energy denoted as E_{pu} and related to the carrier concentration and its effective mass, and the damping coefficient denoted as Γ_D and related to various scattering mechanisms of free electrons. Formally, we are using the following equation:

$$\varepsilon_{\mathrm{Drude}}(E) = \varepsilon_\infty + \frac{E_{pu}^2}{-E^2 - iE\Gamma_D}, \tag{1}$$

where E stands for the photon energy, and i stands for the imaginary unit. As can be seen in Fig. 4d, the average value of the plasma energy increases when the Ar flow decreases from 100 to 25 sccm, but when the Ar flow reaches 10 sccm, the E_{pu} seems to decrease slightly, at least for the stoichiometric samples. Similarly behaves

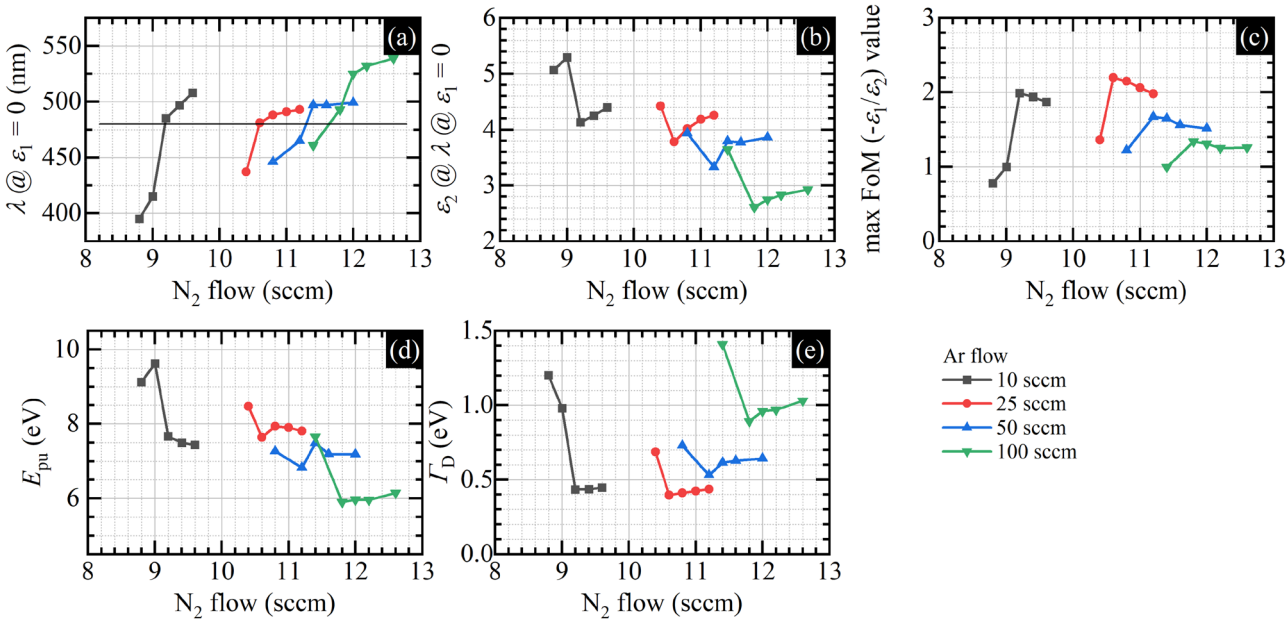

Figure 4. (**a**) Wavelength at which the real part of the dielectric function equals zero, (**b**) imaginary part of the dielectric function at the wavelength at which the real part of the dielectric function equals zero, (**c**) maximum values of the plasmonic Figure of Merit, (**d**) plasma energy in the Drude model, and (**e**) related damping coefficient of TiN films as a function of N_2 flow for different Ar flow values.

the Drude damping coefficient plotted in Fig. 4e—its value decreases when the Ar flow decreases from 100 to 25 sccm, but when the Ar flow reaches 10 sccm, the Γ_D seems to increase its value slightly. So the low-pressure sputtering, which means increased surface bombardment by the high-energy particles, might improve the average metallicity of the TiN film, at least to some point. However, simultaneously progressive amorphization, which also means a decrease in the average nanocrystallite size as the working pressure decreases, may lead to breaking down this positive trend for the smallest nanocrystallites, as seen in the example of the data acquired for the 10 sccm Ar flow.

We also note that the last conclusion partially aligns with the literature that reports the decrease in the resistivity value as the working pressure during the deposition of the TiN samples decreases[43]. However, since the sputtering pressure in the cited work is decreased from 0.65 Pa to only 0.13 Pa, only the positive effect of the lower working pressure (decrease in the resistivity value) is observed. In our work, we are able to grasp the breaking down of the positive influence of lower working pressure because the minimal value of the pressure equals 0.013 Pa, one order of magnitude lower than in the cited work.

Evolution of the plasmonic properties of the stoichiometric titanium nitride films with thickness

In the second part of our experiment, we analyze how the deposition time in the employed physical vapor deposition system, which translates directly into films' thickness, influences the optical properties of the stoichiometric films characterized by the different microstructures.

Figure 5 shows data helpful for qualitative analysis. The SEM images of the thickest samples (2.2 µm, 2.1 µm, 3.1 µm, and 3.3 µm) shown in Fig. 5a–d reveal columnar structure without any significant changes during deposition, and the AFM images shown in Fig. 5e–h illustrate the surface topography with clear evolution of the surface faceting. The real part of the dielectric function shown in Fig. 5i–l seems to not depend significantly on the films' thickness but depends on the microstructure. The imaginary part of the dielectric function, shown in Fig. 5m–p, on the other hand, depends both on the films' thickness and microstructure. Consequently, the plasmonic figure of merit depends on the microstructure and films' thickness. To analyze these data quantitively, we plotted selected parameters characterizing the dielectric function in Fig. 6.

Figure 6a shows maximal values of the Figure of Merit for samples obtained for varying deposition time that directly translates into the films' thickness for all four series of Ar flow. As can be seen, the plasmonic properties improve with the films' thickness, particularly, exponential saturation of the plasmonic Figure of Merit versus the films' thickness can be observed (the solid line in Fig. 6a is the fitted exponential function). Similarly to the first part of our experiment, samples characterized by the best plasmonic properties were deposited with 25 sccm Ar flow, and the plasmonic figure of merit for series deposited with lower (10 sccm) and higher (50 sccm, 100 sccm) Ar flow is worse. Thus, the shown data allow for upholding the thesis on the influence of the microstructure on plasmonic properties. Our result in part related to the thickness dependence is qualitatively similar to the result obtained for TiN film grown using the ALD method on a sapphire substrate at 450 °C and which was interpreted as the effect of lower quality of the layers near the substrate and the increase of the broadly understood quality as the thickness increases[16]. We note, however, that in the cited work, the thickness of the films equals up to 100 nm,

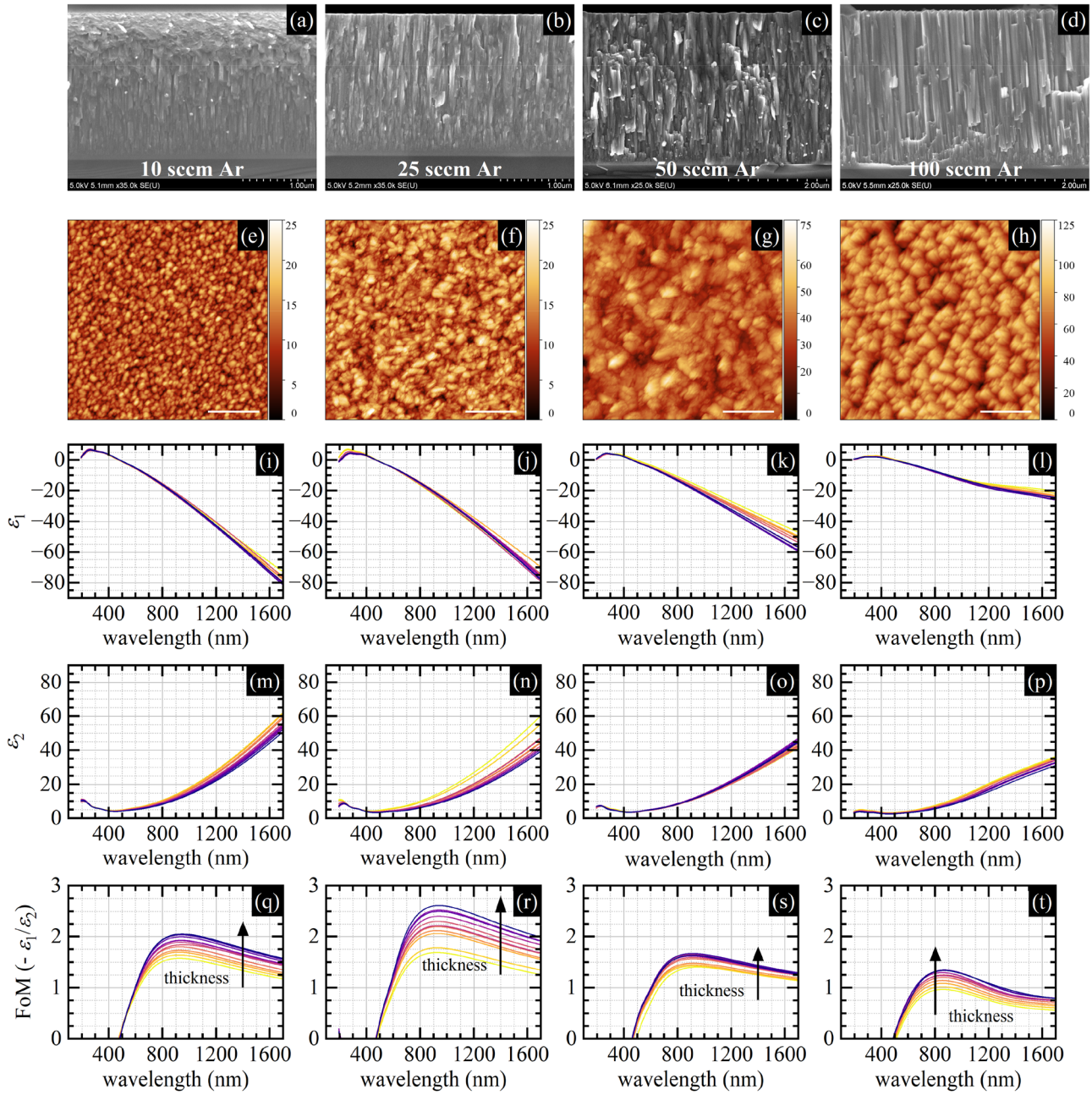

Figure 5. (**a**–**d**) SEM pictures, (**e**–**h**) AFM pictures (the length of the scale bar equals 500 nm), (**i**–**l**) real ε_1 part of the dielectric function, (**m**–**p**) imaginary ε_2 part of the dielectric function, and (**q**–**t**) the plasmonic Figure of Merit ($-\varepsilon_1/\varepsilon_2$) as a function of wavelength for different thickness values (within the plots) and Ar flows (between the plots).

whereas in our case, it is in the micrometer range; particularly for our samples, the saturation/stabilization of the plasmonic figure of merit occurs for films thicker than 1 μm.

Figure 6b illustrates changes in the RMS value as a function of thickness. A linear increase in the film's roughness is observed, and the surface roughness for the selected thickness correlates with the working pressure at which the samples were deposited—the lower the pressure, the lower the roughness. So, the RMS data correlate well with the nanocrystallite size calculated from the XRD spectra. The increase in the surface roughness as the thickness increases is a typical observation. The possible explanations include the accumulation of the effect of the structural defects and increased grain size.

To provide further insight into made observations, we analyze the plasma energy value and the damping coefficient from the Drude model shown in Fig. 6c,d, respectively. The plasma energy value decreases with thickness for samples deposited with the 10 sccm, 25 sccm, and 100 sccm Ar flow, whereas the results for the 50 sccm Ar flow are ambiguous. The Drude damping coefficient exponentially decreases with thickness for all Ar flow values (the solid line in Fig. 6d is the fitted exponential function). A decrease in plasma energy means a decrease in the averaged film metallicity, which seems to be a rather negative effect. In contrast, a decrease in

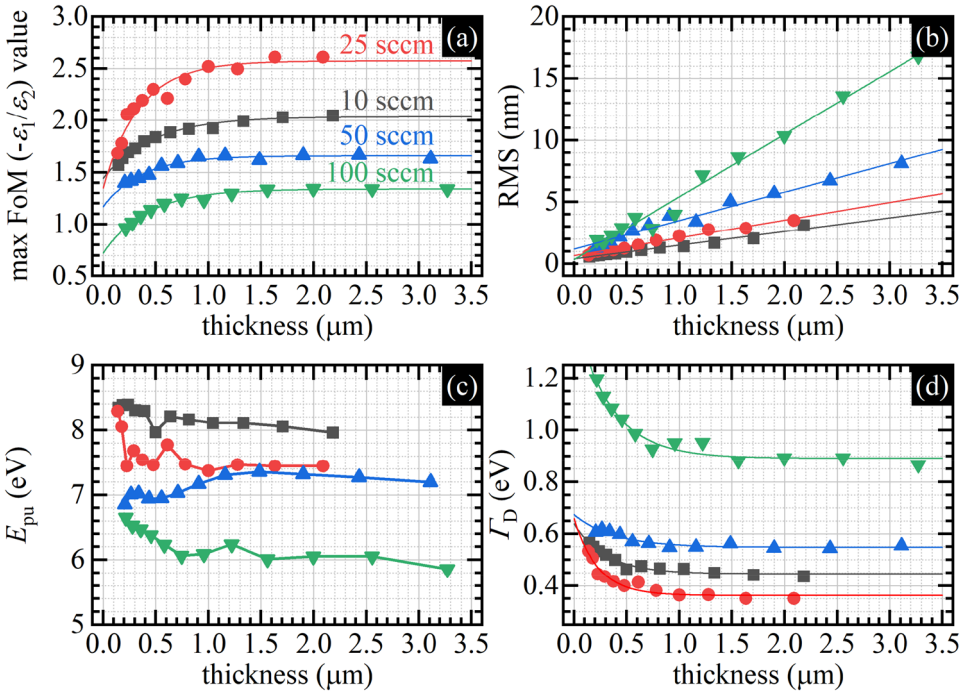

Figure 6. (**a**) Maximum values of the plasmonic Figure of Merit, (**b**) RMS, (**c**) plasma energy in the Drude model, and (**d**) related damping coefficient of TiN films as a function of films' thickness for different Ar flow values.

the damping coefficient means a decrease in the scattering rate, which is a positive effect. Similar effects have been reported by Saha et al.[33] for the polycrystalline TiN films deposited on silicon at 800 °C with thicknesses up to 200 nm. The interpretation was that the increased grain size for thicker samples results in reduced collisions of charge carriers within the grains (the decrease in the damping constant), and the columnar growth with many grain boundaries results in reduced film density and facilitates the oxygen diffusion into the TiN film (the decrease in the plasma energy). This interpretation is also possible for our results since it is supported, e.g., by the surface roughness analysis. Still, other explanations, also those related to process and technology details, are not undoubtedly excluded[45]. Nevertheless, additional structural analysis using STEM microscopy has been performed for the thickest layer deposited with the 25 Ar flow to check if grain size indeed changes during the deposition process, as suspected.

As revealed in Fig. 7a, the structure of the deposited polycrystalline layer consists of ultrafine elongated grains with a size that depends on the distance from the substrate (deposition time). The smallest grains can be found at the interface with the substrate, and as the layer becomes thicker, the grain size increases, reaching its maximum near the surface. Figure 7b–d show three high-resolution images taken near the interface, in the middle of the layer, and near the surface. These images were transformed using the Fast Fourier Transform (FFT) to get diffraction patterns, shown in Fig. 7e–g. These patterns are very complex due to the high density of structural defects and low-angle grain boundaries, and thus, rigorous interpretation is impossible without numerical analysis. However, still some semi-qualitative analysis can be performed. At the interface with the substrate, the FFT diffraction pattern (Fig. 7g) is characterized by continuous rings, which suggests a high number of small grains. Their thickness was estimated to be in the 8–12 nm range, and their length was estimated not to exceed 50 nm. These grains are elongated along the growth direction. In the middle of the sample, 50 nm thick and 200 nm long grains can be found, but we note that despite the increase in the typical grain size, these larger grains are still surrounded by smaller grains. The rings in Fig. 7f became discontinuous, meaning the number of grains decreased in the scanning area significantly compared to the interface. Near the surface, the grain size increases even more, and the rings in Fig. 7e are even more discontinuous when compared to Fig. 7f. The individual bright spots in the FFT diffraction pattern can be attributed to 200 nm thick and 500 nm long grains that can be occasionally identified. But as in the middle of the sample, they are still surrounded by smaller grains. Our direct observations of the increase in the grain size are an expected result and are in line with previous literature reports. However, recalling the optical context of our work, it is the first demonstration of a correlation between the grain size evolution and changes in the plasmonic performance of the films.

Plasmonic gratings on the surface of titanium nitride thick film

One of our work aims is to develop a silicon technology-compatible substrate with plasmonic properties competitive with gold and silver that can be further safely processed, e.g., structurized. Therefore, in this subchapter, we theoretically analyze the optical response (reflection vs. wavelength) of one-dimensional plasmonic grating[46] fabricated on the surface of the titanium nitride thick/nontransparent film. For simulations with Comsol

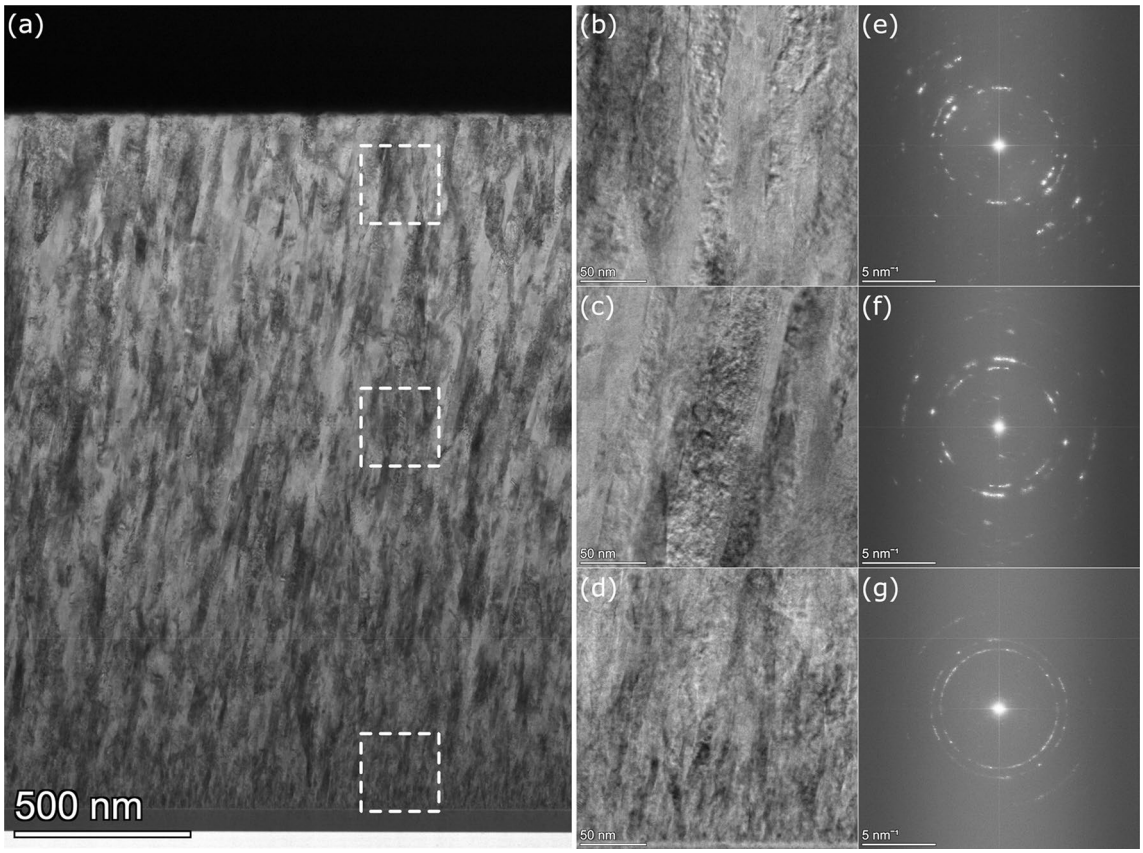

Figure 7. (**a**) STEM picture of the cross-section of the thickest sample deposited with 25 Ar flow; (**b**–**d**) zooms of the areas near the surface, in the middle of the layer, and near the substrate; (**e**–**g**) corresponding FFT diffraction patterns.

Multiphysics, we used the dielectric function describing the thickest TiN film deposited with 25 sccm Ar flow. The Drude parameters equal $E_{pu} = 7.4$eV and $\Gamma_D = 0.35$eV, and the corresponding refractive index n and extinction coefficient k are shown in Fig. 8a. The blue region indicates the spectral range for which $n < 1$, i.e., approximately from 520 nm up to 1020 nm. The simulated plasmonic grating is assumed to consist of an infinite one-dimensional array of rectangular cross-section infinite nanogrooves that are etched on the surface of the infinite (thick enough/nontransparent) TiN substrate with the following dimensions: the period equals 500 nm, the depth of the nanogroove equals 70 nm, and the width varies from 40 to 400 nm. Exemplary electric field distribution when the polarization of the incident light is parallel (TE) and perpendicular to the nanogrooves (TM) within one unit cell is shown in Fig. 8b, whereas the simulated reflection values at normal incidence are shown in Fig. 8c. The presented data clearly demonstrate surface plasmon resonance (SPR) excitation manifested by the minimum reflection occurring only for the TM polarization. The presence of the grating assures momentum matching of the surface plasmon-polaritons (SPPs) and the incident photons, and the efficiency of

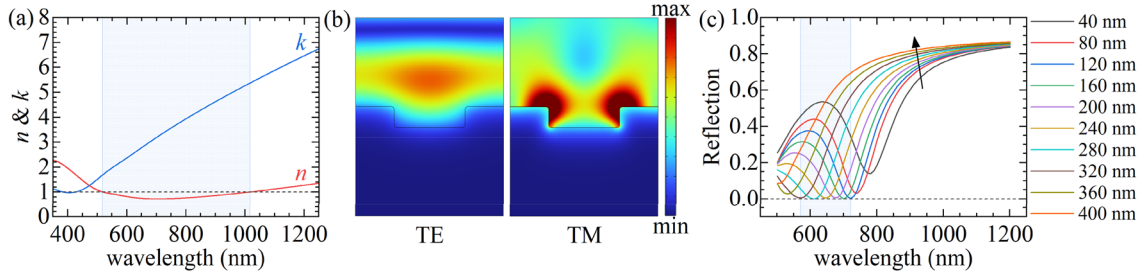

Figure 8. (**a**) Refractive index n and extinction coefficient k for sample possessing best plasmonic properties, the blue region indicates spectral range when $n < 1$, (**b**) electric field distribution when the polarization of the incident light is parallel (TE) and perpendicular to the nanogrooves (TM), (**c**) simulated reflection coefficient from plasmonic grating during normal incidence when the electric field is perpendicular to the nanogrooves, the blue region indicates the spectral range for which null reflection at particular wavelength can be observed.

the photon-plasmon coupling for a given grating period can be optimized by the adjustment of a nanogroove width. For optimal conditions, the energy of the incident wave is totally transferred to the propagating surface mode, resulting in zero reflection at the resonant wavelength (approximately from 570 to 720 nm). These results confirm that the optimized material might be an excellent counterpart of the noble metals for fabricating plasmon-enhanced devices functional in the VIS–NIR spectral range.

Structurization of the developed material might also be used to fabricate the nanostructures allowing the excitation of localized surface plasmons (LSPs) exhibiting stronger light confinement at the metal–dielectric interface in comparison to the propagating SPP modes. For example, localized surface plasmon resonance (LSPR) with null reflection at a particular wavelength has been recently experimentally demonstrated for the HfN nanodisk array[47].

Conclusions

We demonstrate an optimization strategy for depositing relatively thick titanium nitride film with competitive plasmonic properties at room temperature onto a non-matched substrate. We exploit the fact that proper control of the selected process parameters allows for controlling the films' stoichiometry, microstructure, and thickness—three properties that significantly influence the optical properties of polycrystalline titanium nitride films. Consequently, the sample with the best plasmonic properties is characterized by a maximum FoM value of 2.6 and FoM value of 2.1 at 700 nm and 1550 nm. Simultaneously, we made four interesting observations that shed some light on the physical phenomena occurring during the deposition process. The first two are related to the fact that working pressure control through Ar flow control determines the kinetic energy distribution in the particle flux approaching and impacting the substrate. Thus, as the working pressure decreases, we are observing the increase in the averaged metallicity of the films, understood as the increase in the Drude plasma energy value, and the progressive amorphization understood as the decrease in the average nanocrystallite size and the emergence of random nanocrystallite orientation. The last two observations are related to the changes in the film surface as the film thickness increases: a decrease in the averaged metallicity of the films, which seems to be a negative effect, and a decrease in the damping constant, which is a positive effect. Both originate from the directly observed increase in the grain size as the deposition time increases.

Experimental

Deposition of the TiN films

All titanium nitride films were deposited using a pulsed-DC reactive magnetron sputtering technique in the Oxford Plasmalab System 400 Sputter tool. The Advanced Energy Pinnacle Plus + power supply (100 kHz pulsing frequency and 4 μs off-time) delivered the power to the chamber. The deposition was performed at room temperature; however, some non-essential and non-intentional sample heating was observed during the deposition. The sputtering was performed from a pure 8 inches diameter titanium target. Argon was the main sputtering gas, whereas adding gaseous nitrogen made the deposition process reactive. The chamber base pressure value was below 5.0×10^{-7} Torr before and after every deposition. During the deposition process, the pressure was not controlled by the pressure controller but by the Ar flow. The exact values of the working pressure are below 0.1 mTorr (below 0.013 Pa) for 10 sccm Ar flow, 0.3 mTorr (0.04 Pa) for 25 sccm Ar flow, 1.1 mTorr (0.15 Pa) for 50 sccm Ar flow, and 2.7 mTorr (0.36 Pa) for 100 sccm Ar flow.

All reported in this paper titanium nitride films were deposited on a typical silicon wafer with (100) orientation. However, the crystalline titanium nitride films deposited in our system directly on the monocrystalline silicon substrate (even with the native oxide layer) are characterized by enormous stress, which typically leads to damage through cracking. Thus, a 10 nm thick TiO_x interlayer was deposited on the silicon wafer before the proper titanium nitride film was deposited to mitigate this problem.

Characterization

Surface topography was investigated using Bruker Dimension Icon Atomic Force Microscope in the ScanAsyst mode. Scan areas are set to 2 μm × 2 μm (512 points × 512 points).

The X-Ray diffraction (XRD) measurements were performed with the PANalytical X'Pert Pro MRD diffractometer equipped with the radiation-generating tube of the wavelength of 1.54056 Å, a hybrid two-bounce Ge (220) monochromator and a PIXcel detector with the parallel plate collimator with the 0.4-rad Soller slits and a 0.18-deg divergence slit. All scans were performed in Bragg–Brentano geometry. The peak profiles in the XRD patterns were described by the Voigt function. The empirical Sherrer's formula was employed to estimate the size of the nanocrystallites. Since all the raw XRD patterns are dominated by the silicon (400) reflection from the (100) oriented substrate, the (400) reflection was numerically subtracted from all the XRD patterns to make the plots more readable. Next, the patterns were baseline-corrected and normalized to the titanium nitride (111) peak.

For the TEM observations, the FIB lamella was prepared by the lift-out technique perpendicular to the sample surface. The microstructure observations were performed by using the HR TEM/STEM microscope model Spectra 200 made by Thermo Fisher Scientific. The observations were carried out at 200 kV in STEM mode using HAADF and BF detectors. The Fast Fourier Transform was obtained from high-resolution images.

Optical characterization was performed using Woollam RC2 spectroscopic ellipsometer. The $\Psi(\lambda)$ and $\Delta(\lambda)$ parameters were recorded in the range of 193–1690 nm for the following incident angles: 45°, 50°, 55°, 60°, 65°, 70°, and 75°. Modeling of the optical properties was performed in CompleteEASE software. Although most of the fabricated TiN_x layers are expected to be opaque, some slight influence of the substrate on the extracted dielectric function was observed for the thinnest samples. Thus, in order not to introduce additional uncertainty related to the change of the optical model for different samples, our optical model takes into account all the constituents of the investigated structure, i.e., Si substrate, native SiO_2 layer, TiO_x interlayer, the TiN_x layer, and the roughness for all the samples. Dielectric constants of Si, SiO_2, and TiO_x are taken from the Woollam database, while TiN_x

dielectric function is modeled with the use of the General Oscillator model where the real part of the permittivity is described by the e_∞ that is permittivity at an infinite frequency and two poles that are equivalent to a Lorentz oscillator with zero broadening, that are placed outside of the measured spectral range. The imaginary part of permittivity in the UV–Vis is described by four Lorentz oscillators, and the metallic properties in the NIR range are parametrized by the Drude oscillator. The roughness is modeled as an effective layer assuming 50% content of voids and underlying material, and its optical constants are calculated using the Bruggeman Effective Medium Approximation. It is worth mentioning that although the measured TiN_x samples might be considered semi-infinite, the pseudo-dielectric function approximation is not applicable in our case. First, because our samples are nontransparent and highly absorbing, thus the whole ellipsometric information is acquired from the surface. Second, the surface roughness characterizing our samples is large enough to introduce differences between the results obtained using the pseudodielectric approximation and the different ellipsometric models that try to include the effect of finite surface roughness. Further discussion can be found in the Supplementary Information.

Data availability

Data sets generated and/or analyzed during the current study are available from the corresponding author on reasonable request.

Received: 23 May 2023; Accepted: 6 March 2024
Published online: 08 March 2024

References

1. Naik, G. V., Kim, J. & Boltasseva, A. Oxides and nitrides as alternative plasmonic materials in the optical range. *Opt. Mater. Express OME* **1**, 1090–1099. https://doi.org/10.1364/OME.1.001090 (2011).
2. Naik, G. V. *et al.* Titanium nitride as a plasmonic material for visible and near-infrared wavelengths. *Opt. Mater. Express* **2**, 478. https://doi.org/10.1364/OME.2.000478 (2012).
3. Patsalas, P., Kalfagiannis, N. & Kassavetis, S. Optical properties and plasmonic performance of titanium nitride. *Materials* **8**, 3128–3154. https://doi.org/10.3390/ma8063128 (2015).
4. Naik, G. V., Shalaev, V. M. & Boltasseva, A. Alternative plasmonic materials: Beyond gold and silver. *Adv. Mater.* **25**, 3264–3294. https://doi.org/10.1002/adma.201205076 (2013).
5. Guler, U., Boltasseva, A. & Shalaev, V. M. Refractory plasmonics. *Science* **344**, 263–264. https://doi.org/10.1126/science.1252722 (2014).
6. Tripura Sundari, S., Ramaseshan, R., Jose, F., Dash, S. & Tyagi, A. K. Investigation of temperature dependent dielectric constant of a sputtered TiN thin film by spectroscopic ellipsometry. *J. Appl. Phys.* **115**, 033516. https://doi.org/10.1063/1.4862485 (2014).
7. Reddy, H. *et al.* Temperature-dependent optical properties of plasmonic titanium nitride thin films. *ACS Photon.* **4**, 1413–1420. https://doi.org/10.1021/acsphotonics.7b00127 (2017).
8. Krekeler, T. *et al.* Unprecedented thermal stability of plasmonic titanium nitride films up to 1400 °C. *Adv. Opt. Mater.* **9**, 2100323. https://doi.org/10.1002/adom.202100323 (2021).
9. Wells, M. P. *et al.* Temperature stability of thin film refractory plasmonic materials. *Opt. Express* **26**, 15726. https://doi.org/10.1364/OE.26.015726 (2018).
10. Li, W. *et al.* Refractory plasmonics with titanium nitride: Broadband metamaterial absorber. *Adv. Mater.* https://doi.org/10.1002/adma.201401874 (2014).
11. Chaudhuri, K. *et al.* Remote sensing of high temperatures with refractory, direct-contact optical metacavity. *ACS Photon.* **7**, 472–479. https://doi.org/10.1021/acsphotonics.9b01450 (2020).
12. Gadalla, M. N., Greenspon, A. S., Tamagnone, M., Capasso, F. & Hu, E. L. excitation of strong localized surface plasmon resonances in highly metallic titanium nitride nano-antennas for stable performance at elevated temperatures. *ACS Appl. Nano Mater.* **2**, 3444–3452. https://doi.org/10.1021/acsanm.9b00370 (2019).
13. Langereis, E., Heil, S. B. S., van de Sanden, M. C. M. & Kessels, W. M. M. In situ spectroscopic ellipsometry study on the growth of ultrathin TiN films by plasma-assisted atomic layer deposition. *J. Appl. Phys.* **100**, 023534. https://doi.org/10.1063/1.2214438 (2006).
14. Van Bui, H. *et al.* Growth kinetics and oxidation mechanism of ALD TiN Thin films monitored by in situ spectroscopic ellipsometry. *J. Electrochem. Soc.* **158**, H214. https://doi.org/10.1149/1.3530090 (2011).
15. Briggs, J. A. *et al.* Fully CMOS-compatible titanium nitride nanoantennas. *Appl. Phys. Lett.* **108**, 051110. https://doi.org/10.1063/1.4941413 (2016).
16. Fomra, D. *et al.* Plasmonic titanium nitride via atomic layer deposition: A low-temperature route. *J. Appl. Phys.* **127**, 103101. https://doi.org/10.1063/1.5130889 (2020).
17. Murai, S. *et al.* Plasmonic arrays of titanium nitride nanoparticles fabricated from epitaxial thin films. *Opt. Express* **24**, 1143. https://doi.org/10.1364/OE.24.001143 (2016).
18. Sugavaneshwar, R. P. *et al.* Fabrication of highly metallic tin films by pulsed laser deposition method for plasmonic applications. *ACS Photon.* **5**, 814–819. https://doi.org/10.1021/acsphotonics.7b00942 (2018).
19. Guo, W.-P. *et al.* Titanium nitride epitaxial films as a plasmonic material platform: Alternative to gold. *ACS Photon.* **6**, 1848–1854. https://doi.org/10.1021/acsphotonics.9b00617 (2019).
20. Maurya, K. C., Shalaev, V. M., Boltasseva, A. & Saha, B. Reduced optical losses in refractory plasmonic titanium nitride thin films deposited with molecular beam epitaxy. *Opt. Mater. Express* **10**, 2679. https://doi.org/10.1364/OME.405259 (2020).
21. Adachi, S. & Takahashi, M. Optical properties of TiN films deposited by direct current reactive sputtering. *J. Appl. Phys.* **87**, 1264–1269. https://doi.org/10.1063/1.372006 (2000).
22. Zgrabik, C. M. & Hu, E. L. Optimization of sputtered titanium nitride as a tunable metal for plasmonic applications. *Opt. Mater. Express* **5**, 2786. https://doi.org/10.1364/OME.5.002786 (2015).
23. Yang, Z.-Y., Chen, Y.-H., Liao, B.-H. & Chen, K.-P. Room temperature fabrication of titanium nitride thin films as plasmonic materials by high-power impulse magnetron sputtering. *Opt. Mater. Express* **6**, 540. https://doi.org/10.1364/OME.6.000540 (2016).
24. Chang, C.-C. *et al.* Highly Plasmonic titanium nitride by room-temperature sputtering. *Sci. Rep.* **9**, 15287. https://doi.org/10.1038/s41598-019-51236-3 (2019).
25. Mascaretti, L. *et al.* Controlling the plasmonic properties of titanium nitride thin films by radiofrequency substrate biasing in magnetron sputtering. *Appl. Surface Sci.* **554**, 149543. https://doi.org/10.1016/j.apsusc.2021.149543 (2021).
26. Promjantuk, T. *et al.* Spectroscopic study on alternative plasmonic TiN-NRs film prepared by R-HiPIMS with GLAD technique. *Radiat. Phys. Chem.* **202**, 110589. https://doi.org/10.1016/j.radphyschem.2022.110589 (2023).
27. Bower, R. *et al.* Complementary metal–oxide–semiconductor compatible deposition of nanoscale transition-metal nitride thin films for Plasmonic applications. *ACS Appl. Mater. Interfaces* **12**, 45444–45452. https://doi.org/10.1021/acsami.0c10570 (2020).

28. Zhang, R. *et al.* Wafer-scale epitaxy of flexible nitride films with superior plasmonic and superconducting performance. *ACS Appl. Mater. Interfaces* **13**, 60182–60191. https://doi.org/10.1021/acsami.1c18278 (2021).
29. Zhang, R. *et al.* Crystal orientation-dependent oxidation of epitaxial TiN films with tunable plasmonics. *ACS Photon.* **8**, 847–856. https://doi.org/10.1021/acsphotonics.0c01827 (2021).
30. Ding, K. *et al.* A platform for complementary metal–oxide–semiconductor compatible plasmonics: High plasmonic quality titanium nitride thin films on Si (001) with a MgO interlayer. *Adv Photo Res.* **2**, 2000210. https://doi.org/10.1002/adpr.202000210 (2021).
31. Bi, J. *et al.* Robust plasmonic properties of epitaxial TiN films on highly lattice-mismatched complex oxides. *Phys. Rev. Mater.* **5**, 075201. https://doi.org/10.1103/PhysRevMaterials.5.075201 (2021).
32. Shah, D. *et al.* Thickness-dependent drude plasma frequency in transdimensional plasmonic TiN. *Nano Lett.* **22**, 4622–4629. https://doi.org/10.1021/acs.nanolett.1c04692 (2022).
33. Saha, S. *et al.* Tailoring the thickness-dependent optical properties of conducting nitrides and oxides for epsilon-near-zero-enhanced photonic applications. *Adv. Mater.* https://doi.org/10.1002/adma.202109546 (2022).
34. Movchan, B. A. & Demshishin, A. V. Structure and properties of thick condensates of nickel, titanium, tungsten, aluminum oxides, and zirconium dioxide in vacuum. *Fiz. Met. Metalloved.* **28**, 653 (1969).
35. Thornton, J. A. Influence of apparatus geometry and deposition conditions on the structure and topography of thick sputtered coatings. *J. Vacuum Sci. Technol.* **11**, 666–670. https://doi.org/10.1116/1.1312732 (1974).
36. Mahieu, S., Ghekiere, P., Depla, D. & De Gryse, R. Biaxial alignment in sputter deposited thin films. *Thin Solid Films* **515**, 1229–1249. https://doi.org/10.1016/j.tsf.2006.06.027 (2006).
37. Mahieu, S. & Depla, D. Reactive sputter deposition of TiN layers: modelling the growth by characterization of particle fluxes towards the substrate. *J. Phys. D: Appl. Phys.* **42**, 053002. https://doi.org/10.1088/0022-3727/42/5/053002 (2009).
38. Anders, A. A structure zone diagram including plasma-based deposition and ion etching. *Thin Solid Films* **518**, 4087–4090. https://doi.org/10.1016/j.tsf.2009.10.145 (2010).
39. Johansson, F. O. L. *et al.* Minimizing sputter-induced damage during deposition of WS_2 onto graphene. *Appl. Phys. Lett.* **110**, 091601. https://doi.org/10.1063/1.4977709 (2017).
40. Pliatsikas, N. *et al.* Energetic bombardment and defect generation during magnetron-sputter-deposition of metal layers on graphene. *Appl. Surface Sci.* **566**, 150661. https://doi.org/10.1016/j.apsusc.2021.150661 (2021).
41. Smith, H. A. *et al.* Epitaxial titanium nitride on sapphire: Effects of substrate temperature on microstructure and optical properties. *J. Vacuum Sci. Technol. A.* **36**, 03E107. https://doi.org/10.1116/1.5022068 (2018).
42. Judek, J. *et al.* Titanium nitride as a plasmonic material from near-ultraviolet to very-long-wavelength infrared range. *Materials* **14**, 7095. https://doi.org/10.3390/ma14227095 (2021).
43. Yeh, T.-S., Wu, J.-M. & Hu, L.-J. The properties of TiN thin films deposited by pulsed direct current magnetron sputtering. *Thin Solid Films* **516**, 7294–7298. https://doi.org/10.1016/j.tsf.2008.01.001 (2008).
44. Doiron, B. *et al.* Quantifying figures of merit for localized surface plasmon resonance applications: A materials survey. *ACS Photon.* **6**, 240–259. https://doi.org/10.1021/acsphotonics.8b01369 (2019).
45. Braic, L. *et al.* Titanium oxynitride thin films with tunable double epsilon-near-zero behavior for nanophotonic applications. *ACS Appl. Mater. Interfaces* **9**, 29857–29862. https://doi.org/10.1021/acsami.7b07660 (2017).
46. Gadalla, M. N., Chaudhary, K., Zgrabik, C. M., Capasso, F. & Hu, E. L. Imaging of surface plasmon polaritons in low-loss highly metallic titanium nitride thin films in visible and infrared regimes. *Opt. Express* **28**, 14536. https://doi.org/10.1364/OE.391482 (2020).
47. Chiao, Z.-Y. *et al.* Full-color generation enabled by refractory plasmonic crystals. *Nanophotonics* **11**, 2891–2899. https://doi.org/10.1515/nanoph-2022-0071 (2022).

Acknowledgements

This work was supported by the POB FOTECH-3 project entitled "Plasmons and polaritons on nanostructured surfaces of IVb metal nitrides" granted by the Warsaw University of Technology within "The Excellence Initiative—Research University" program.

Author contributions

M.N.: Investigation, Data Curation, writing—original draft, writing—review and editing; C.J.: Investigation, writing—review and editing; T.P.: Investigation, writing—review and editing; P.W.: Methodology, Formal analysis, investigation, writing—original draft, writing—review and editing; A.S.: Investigation, Writing—review and editing; J.J.: Conceptualization, methodology, writing—original draft, writing—review and editing, supervision, project administration, funding acquisition.

Competing interests

The authors declare no competing interests.

Additional information

Supplementary Information The online version contains supplementary material available at https://doi.org/10.1038/s41598-024-56406-6.

Correspondence and requests for materials should be addressed to J.J.